Demodulations of Fiber Optical Sensors using Buneman Frequency Analysis for High Temperature Sensing Applications

by

Chengqi Zhu

Bachelor of Engineering, China Jiliang University, 2018

Submitted to the Graduate Faculty of the

Swanson School of Engineering in partial fulfillment

of the requirements for the degree of

Master of Science

University of Pittsburgh

2020

UNIVERSITY OF PITTSBURGH

SWANSON SCHOOL OF ENGINEERING

This thesis was presented

by

Chengqi Zhu

It was defended on

September 28, 2020

and approved by

Kevin P. Chen, Ph.D., Professor, Department of Electrical and Computer Engineering

Zhi-Hong Mao, Ph.D., Professor, Department of Electrical and Computer Engineering

Feng Xiong, Ph.D., Assistant Professor, Department of Electrical and Computer Engineering

Thesis Advisor: Kevin P. Chen, Ph.D., Professor, Department of Electrical and Computer
Engineering

Demodulations of Fiber Optical Sensors using Buneman Frequency Analysis for High Temperature Sensing Applications

Chengqi Zhu, M.S.

University of Pittsburgh, 2020

Since their inventions, fiber optical sensors (FOSs) have been playing indispensable roles in structure health monitoring. Compared with electronic sensors, FOSs show merit of immunities to electromagnetic fields, resilience in high-temperature harsh environments. The capability of multiplexing many fiber sensors on a single optical fiber makes FOS unique sensor devices to perform distributing sensing.

One of key challenges to perform measurements using fiber sensors is to develop computationally efficient algorithms to demodulate fiber sensors. In this thesis, we explore Buneman frequency estimation (BFE) as a rapid and highly accurate algorithm to determine optical cavity length of multiplexed intrinsic Fabry–Pérot interferometers (IFPIs) and resonance wavelength of Fiber Bragg grating (FBGs). The demodulation algorithm was tested on IFPI sensors with cavity length between 200-μm and 1600-μm. The same demodulation algorithm was also tested on FBG sensors with resonance wavelength around 1550-nm. The computational efficiency and robustness of the new algorithm are compared with a Gaussian FBG peak fitting method. To demonstrate applications of the demodulation algorithm, FBG resonance wavelength in nuclear reactor was tracked for 55 days.

The method presented in this thesis provides a real-time demodulation scheme to track FBG wavelength and to determine optical cavity length changes using low-resolution interrogation

schemes such as low-resolution spectrometers or a tunable laser. It has potential to greatly reduce

the cost of fiber sensor systems.

Table of Contents

List of Tables

List of Figures

Acknowledgement

I would like to express my most sincere gratitude to my advisor, Professor Kevin Chen, for directing me to my own way to do collaborative and independent research as well as supervising my coursework here. Those cheers for each minor progress bring an optimistic attitude to me, which helps me to overcome a lot of difficulties in both academic and daily life through my master program and inspires my spirit for future life.

I want to thank Professor Zhi-hong Mao and Professor Feng Xiong for unconditional supports and help since my first year at the States. I benefit a lot both in and out of class.

I owe special gratitude to Yang Yang and Mohan Wang for so many inspiring suggestions to this work. I also want to thank Jingyu Wu, Qirui Wang, Professor Mohamed Bayoumy and Kehao Zhao for so much beneficial discussion.

Finally, I want to thank my parents for their supports in silence.

1.0 Introduction

Optical fibers were invented in 1960s and have been playing critical roles in information age. As an ultra-low loss and low-cost optical waveguide, optical fibers have revolutionized the transmission and consumption of information and hence change daily life of every single person in the world. In addition to its pivotal role in optical communication, fiber sensors have been widely used for sensing applications. As an optical waveguide that is immune to electromagnetic interference, stable at high temperature and against corrosion, fiber sensors have been considered as excellent measurement devices for harsh environment applications.

A unique trait of fiber optical sensors is their capability to perform high spatial resolution measurements. Fiber sensors based on in-fiber interferometers and fiber Bragg gratings (FBGs) have been widely adopted for structure health monitoring and energy exploration applications. The capability of multiplexing many fiber sensors on one fiber enable high spatial resolution measurement that is unattainable using electronic sensors. Through various functionization process, a wide array of fiber sensors can be developed to perform both physical and chemical measurements such as temperature, strain, pH values, radiation, vibration, gas concentration, and humidity.

Given the harsh environment resilience, fiber sensors have been extensively studied to perform measurements for both fossil fuel energy and nuclear energy industries. Fiber sensors have been shown to be able to withstand extreme temperature up to 1100 ℃ for silica fibers and 1500 ℃ for sapphire fibers. Recent works have shown that optical fibers can withstand extreme strong radiation in nuclear reactor cores. The use of multiplexable fiber sensors to perform high

spatial resolution measurements using one fiber and one fiber feedthrough will significantly increase situation awareness of energy systems leading to safe and efficiency energy production.

One of key challenges of using fiber optical sensors are effective sensor demodulation algorithm. Fiber sensors based on various optical devices such as Fabry-Pérot interferometers or FBGs require computationally intense demodulation algorithms. This impose significant computation burden to extract measurement results from fiber sensors, especially for high frequency measurements. In this thesis, we studies fiber sensor demodulation using a computational efficient Buneman frequency estimation (BFE) method to demodulate two widely used fiber sensor devices. They are intrinsic Fabry-Pérot interferometer (IFPI) and FBGs.

The thesis is organized in five chapters. Chapter 2 introduces operating principles of optical fibers as platform for fiber optical sensing applications. Three types of Fabry-Pérot interferometers with all fiber structures along their fabrication techniques are first introduced. Multiplexable sensors based on fiber Bragg gratings are also introduced. Chapter 3 discusses sensor demodulation methods using BFE method for IFPIs to distinguish multiple fringe orders in cavity length domain. All-phase spectrum is demonstrated to correct time-phase shift for fast Fourier transform (FFT) analysis to obtain accurate results. Chapter 4 focuses on BFE method for rapid demodulation of FBG wavelength and its comparison with traditional Gaussian peak fitting method. To achieve this objective, variances of these two methods and linear fit method are calculated. Chapter 5 presents results of sensor demodulation using experimental data and potential improvement.

2.0 Operation Principles of Fiber Sensors

2.1 Optical Fibers as Waveguide for Light

Optical fibers are ultra-low loss optical waveguide support optical signal and power transmission over long distances. As figure 1 (left) shows, an optical fiber consists of fiber core, cladding and coating layer. Fiber core is the guiding media of light, which is normally made of silica doped with germanium, phosphor, and boron because of its excellent optical transmission over a wide range of wavelengths. Light propagated in optical fiber cores is confined by the principle of total internal reflection.
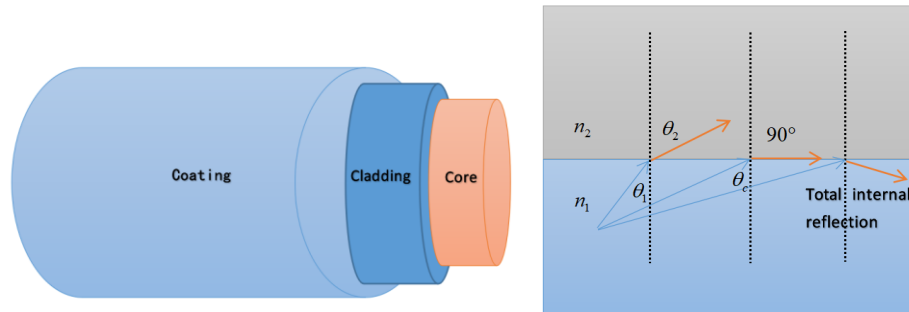
Figure 1 Structure of an Optical Fiber (Left) and Illustration of Total Internal Reflection (Right)

The mechanism is depicted in Figure 1 (right). The critical angle to determine total internal reflection is:

$$\theta_c = arcsin(n_2/n_1) \tag{2.1}$$

It is derived from the law of refraction at the interface of two media with different refractive index is:

$$n_1 \sin \theta_1 = n_2 \sin \theta_2 \qquad (2.2)$$

where θ_1 and θ_2 are incident angle and refraction angle while n_1, n_2 are corresponding refractive index. Since refraction angle never exceeds 90°, once θ_1 exceeds critical angle, incident light will be totally reflected at the surface. The cladding layer has a smaller refractive index than fiber core. By modifying incident angle, light can be confined in the fiber core. Coating is a non-glass layer. A standard coating structure is usually made of a primary and a secondary layer to provide mechanical protection.

By changing size, refractive index contrast, core configurations, and dopant concentration, a great variety of optical fibers have been developed for various applications in lighting, sensing, and data transfer on the board level, in data center, between building, and across continents. Optical fiber can also be excellent platform for sensing devices. In this chapter, we briefly introduce two types of most widely adopted fiber sensors. These include Fabry-Pérot interferometer (FPI) and Fiber Bragg Grating (FBG). In following sections, we provide brief introductions on these two fiber devices.

2.2 Principles of Fabry-Perot Interferometers

Fiber based Fabry-Pérot interferometers (FPIs) are one of the widest used fiber optical sensors. Despite FPIs can be constructed using a wide variety of optical components, general operational principal of FPIs are based on interference of coherent light in an optical resonator. Figure 2 show a schematic sketch of optical resonator formed by two reflectors. When optical

wave is launched into the resonator, the light in the optical resonator incurs multiple reflections form two reflectors as depicted in Figure 2.
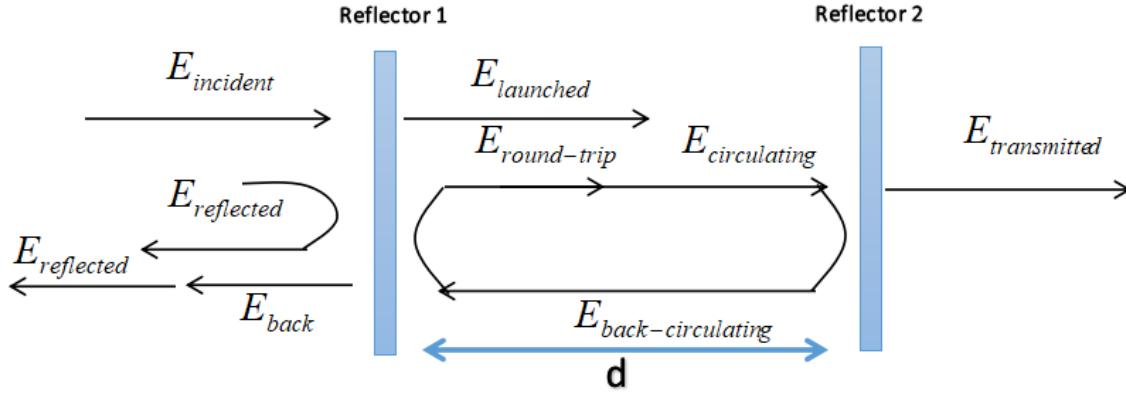
Figure 2 Schematic Sketch of FPI Device

Thus, the optical intensity in the FPI is subject to multi-beam interference theory. As results, the measurable reflectance can be expressed as:

$$A_{refl} = \frac{|E_{reflected}|^2}{|E_{incident}|^2} = \frac{2R(1-\cos\phi)}{1+R^2-R\cos\phi} \tag{2.3}$$

where R denotes reflectivity, ϕ is phase difference incurred by guided light when it travels round distance between two reflectors as $\phi=2\pi nd/\lambda$. This optical phase depends on optical length of the cavity (OL) of two reflectors, which is calculated as:

$$l = nd \tag{2.4}$$

where n is the refractive index of the medium, d is geometric length of the optical cavity, l denotes optical cavity length for the rest of this thesis. Because of low reflectivity of interfaces, higher orders reflections are normally ignored. The interference signal of a fiber-optic FPI is subject to two-beam interference theory by:

5

$$I(\lambda) = 2I_0(\lambda)\left[1 + \gamma \cos\left(\frac{4\pi l}{\lambda} + \pi\right)\right] \tag{2.5}$$

where I_0 is light source, γ denotes fringe visibility for the rest of this thesis. Three types of commonly used fiber based FPIs are designed and engineered. They are extrinsic Fabry–Pérot interferometer (EFPI), intrinsic Fabry–Pérot interferometer (IFPI) and in-line Fabry–Pérot interferometer (in-line FPI). In general, fiber FPIs can be classified into two main categories, extrinsic and intrinsic. The in-line FPI introduced in this thesis can be regarded as a hybrid structure, which combines features of an IFPI and an EFPI. To describe Fabry–Pérot resonator in space. Equation (2.5) can be re-expressed in different forms. All of them as temperature sensors work by tracing optical length path difference:

$$\Delta l = l(\alpha_\Lambda + \alpha_n)\Delta T \tag{2.6}$$

where α_Λ is thermal expansion coefficient, α_n is thermo-optic co-efficient, ΔT is change of temperature. Besides, FPIs are widely adopted as strain sensors [1] [2] or as etalons to characterize specific wavelength in optical cavity.

Compared to other fiber-optic interferometric sensors like Michelson interferometers or Mach-Zehnder interferometers, the interference in FPI is extremely sensitive to external perturbations. In addition, FPIs show merits of compact size and small cross sensitivity, which make them the most widely used one and be adopted in this work as well.

2.2.1 Extrinsic Fabry-Perot Interferometers

The term "extrinsic" refers to the microcavity of fiber FPIs. An EFPI generally utilizes two optical fiber segments bonded with external housing materials. Figure 3 is schematic sketch of one type of EFPI. It is formed by inserting two single mode fibers (SMFs) into a capillary tube to form

6

an air gap. Two interfaces of optical fiber segments and the air gap are essential two reflectors. Interferences occur in the air gap. Optical cavity length is equal to length of the air gap.
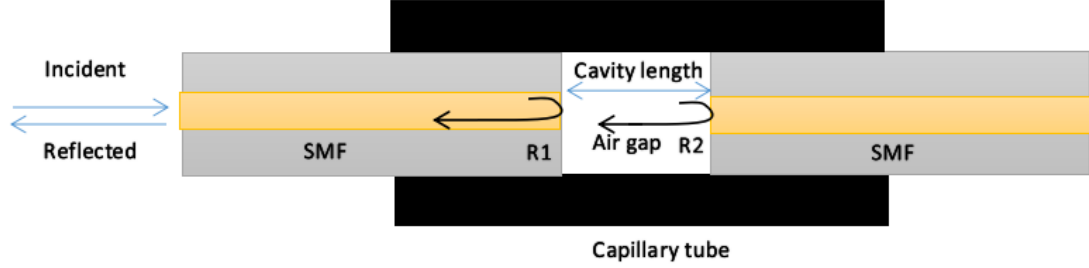
Figure 3 Structure of an Extrinsic Fabry-Pérot Interferometer

A broadband light source is coupled into a fiber and goes through a 2×2 coupler. The light source with two different wavelengths will be launched into the sensor from one side, partial of the light is reflected at the first air-glass interface. The other part transmits through hollow fiber and another partial of propagating light will be reflected at the second interface. Dering from equation (2.5), reflected signal is received from the input side as a function of wavelength [3]:

$$r(\lambda) = A(\lambda) + B(\lambda) \cos\left(\frac{4\pi l}{\lambda}\right) \tag{2.7}$$

where λ is wavelength of injected light, $A(\lambda)$ and $B(\lambda)$ denotes background light and range of the spectrum, which are normally regarded as two constant A_0 and B_0 respectively. After placed in the sensing system, new intensities I_{11} and I_{22} with respect to two different incident wavelengths λ_1 and λ_2 are formed. The optical cavity length changes from l_0 to $l_0 + \Delta l$. The variation of cavity length Δl can be calculated with initial intensities and new intensities with respect to two different incident wavelengths. Wavelength demodulation methods have been explored to demodulate variation of optical cavity length of EFPIs. Wavelength division multiplexing would be indispensable for this type of sensors.

One advantages of EFPIs is their high reflectivity of reflectors compared to other fiber FPIs. Air-glass interfaces in EFPIs have high reflectivity due to large refractive index contrast. Because of this attracting point, EFPIs are widely used in applications other than temperature sensing, such as humidity and acoustic pressure measurement.

2.2.2 Intrinsic Fabry-Perot Interferometers

IFPIs are fabricated by forming reflectors inside a single fiber. One approach to from reflectors in a SMF is by writing a pair of FBGs [4]. However, FBG cascaded IFPIs only produce fringe orders within resonance wavelength, which will affect the precision of demodulation. An IFPI can also be formed by writing a pair of micro-reflectors [5] in the core of a single fiber, which is not bound to the previous trouble. In addition, with type-II grating refractive index change, this type of IFPIs can withstand high temperature. Figure 4 shows a schematic sketch of an IFPI. A broadband light source is launched into the sensor through a circulator. Propagating light will be reflected at two reflecting mirrors in fiber core. IFPIs are integrated with spectrometer to obtain fringe pattern.
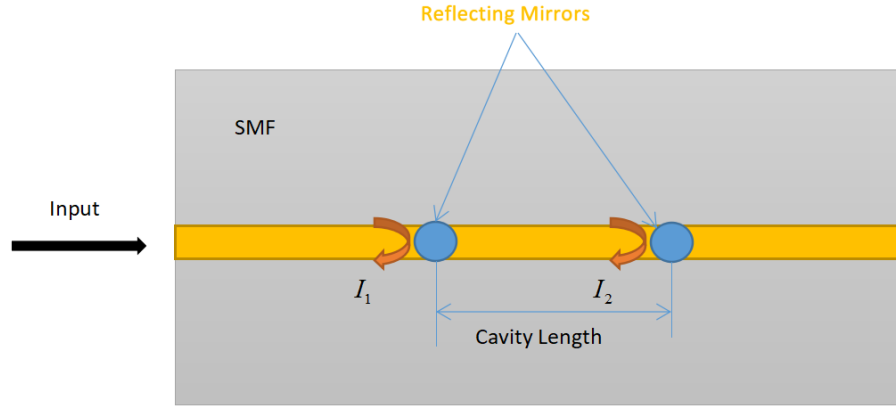
Figure 4 Structure of an Intrinsic Fabry-Pérot Interferometer

According to Wang [6], the interference formula of a white light IFPI can be expressed as a function of wavenumber by:

$$I(k) = 2I_0(k + k_0)[1 + \gamma \cos(2(k + k_0)l + \phi_0)] \qquad (2.8)$$

where k is wavenumber propagating in optical cavity, k_0 is wavenumber of the first data point in spectrum, ϕ_0 is initial phase, which is set as zero in this work since length of reflectors is small enough to be ignored. IFPIs as sensors scan light with optical phase-locked loop to obtain fringe pattern. The IFPI adopted in our experiment is a phase demodulated sensor. Demodulation of IFPIs is with Fourier transform analytic. Signals are transformed from wavenumber domain into spatial frequency domain.

One advantage of IFPIs is their good multiplexing capability. Many pairs of reflectors can be written in a single fiber. The multiplexed sensors perform measurement at different locations. Space division multiplexing (SDM) is an indispensable step for multiplexed IFPIs. This step is briefly introduced in coming section. Besides, an IFPI has lower insertion loss and higher mechanical stability than an EFPI. Thus, it is selected as platform in this work. However, it does

not mean an IFPI is superior to an EFPI in all aspects. Reflecting mirrors in an IFPI do not keep such a high reflectivity as air-glass interfaces in an EFPI due to relatively small refractive index difference.

2.2.3 In-line Fabry-Perot Interferometers

As the name suggests, reflecting mirrors of an in-line FPI are produced by fusion splicing techniques. Sensing elements are cascaded within the fiber. The hybrid structure can be formed by fusing two SMFs with a hollow core fiber or by fusing one SMF and a graded index multimode fiber with a hollow core fiber. An air gap is formed between two optical fiber segments. Figure 5 depicts one type of in-line FPI. The hollow core fiber is normally fabricated by hydrofluoric acid etching and fusion splicing [7]. Propagating light will resonate in the air gap. Interferences are generated at two interfaces.
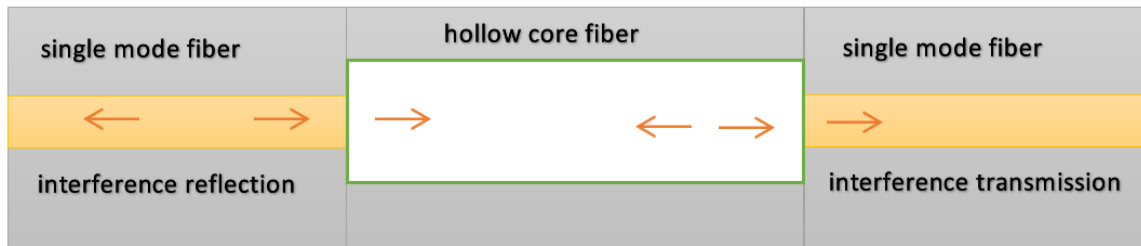
Figure 5 Structure of an In-line Fabry-Pérot Interferometer

With similarity to IFPIs, in-line FPIs as sensors work by tracing phase shift of the interferometric response caused by the change of optical cavity length [8]. These sensors are trade-off between EFPIs and IFPIs in terms of reflectivity, multiplexing capability and other features.

2.2.4 Space Division Multiplexing

Modulation and demodulation are crucial processes in the field of fiber-optic sensing. Modulation varies properties of carrier signals which contain information to be transmitted. Demodulation, on the contrary, provides signals from measured parameters. In a sensing system, spectrum can be detected with electronic devices, such as a charge coupled device (CCD). On the other hand, physical parameters describe how the light behaves. The demodulation process bridges the gap between detectable values and physical parameters.

Multiplexing demodulation is indispensable for FPIs to perform distributing sensing. One of pre-requests for implementing SDM is that cavity lengths of all sensors should differ. In addition, there should be distance between each pair of reflectors to avoid mutual influence, which is also depicted in Figure 6.

Different cavity length
Distance between different pairs of reflectors
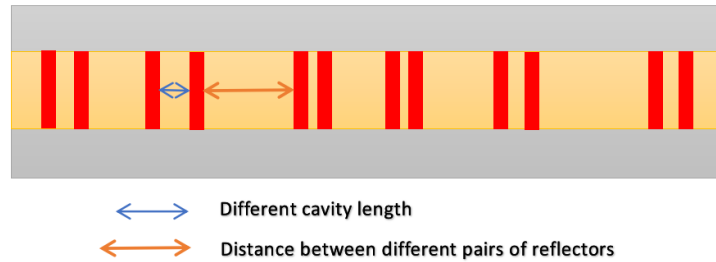
Figure 6 Pre-requests for Implementing Space Division Multiplexing

Figure 7 is a schematic sketch of operating principles of space division multiplexing. The interference spectrum is normally a sinusoidal function (blue line) in wavelength domain. Signals in different channels (yellow lines) correspond to six sensors, which are with different frequency components. They superpose in space to form the interference spectrum. It is not feasible to distinguish all six signals in wavelength domain directly. Signals are transformed from wavelength

11

domain into frequency domain by Fourier transform to obtain fringe orders. Since each pair of reflectors forms different length of optical cavity, amplitude of sensors (green line) can be distinguished in cavity length domain.
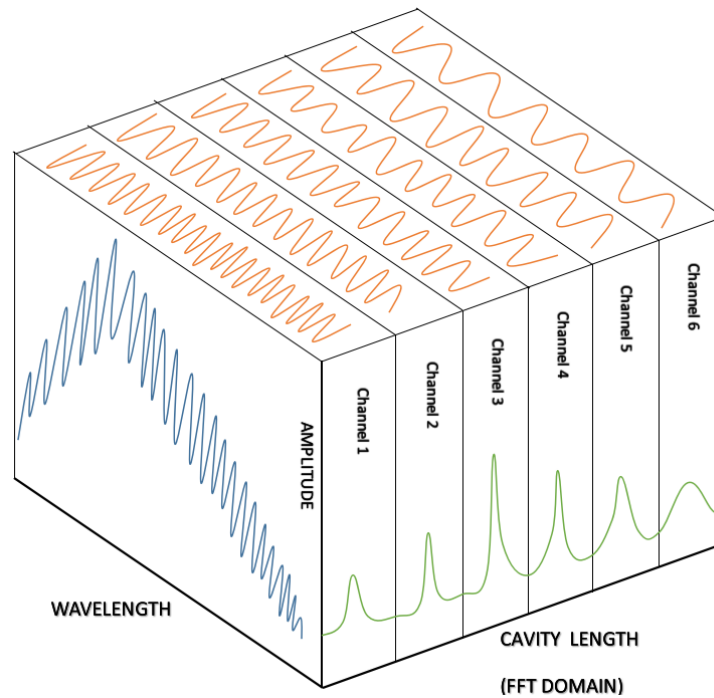
Figure 7 Operating Principles of Space Division Multiplexing

2.3 Fiber Bragg Grating Sensors

Another type of widely used FOSs is fiber Bragg grating (FBG) sensor. The first ever FBG was discovered by Hill et al [9] in 1978. Fiber gratings are consisted of periodic alternation of refractive index of the core. The periodic length of a uniform FBG is constant and refractive index alternation of each period is the same. Propagating light in fiber core will resonate based on the

principle of Bragg diffraction. Bragg diffraction occurs when the wavelength of light is comparable to the distance of two atoms. Bragg condition is defined by:

$$\lambda_{Bragg} = 2n_{eff}\Lambda \qquad (2.9)$$

where n_{eff} is effective refractive index, Λ is the period of index alternation. At each grating, only a rather small part of light will be reflected. The other part will transmit through the grating as Figure 8 shows. Many of gratings are written on a single fiber. Thus, reflection in FBGs increases periodically.
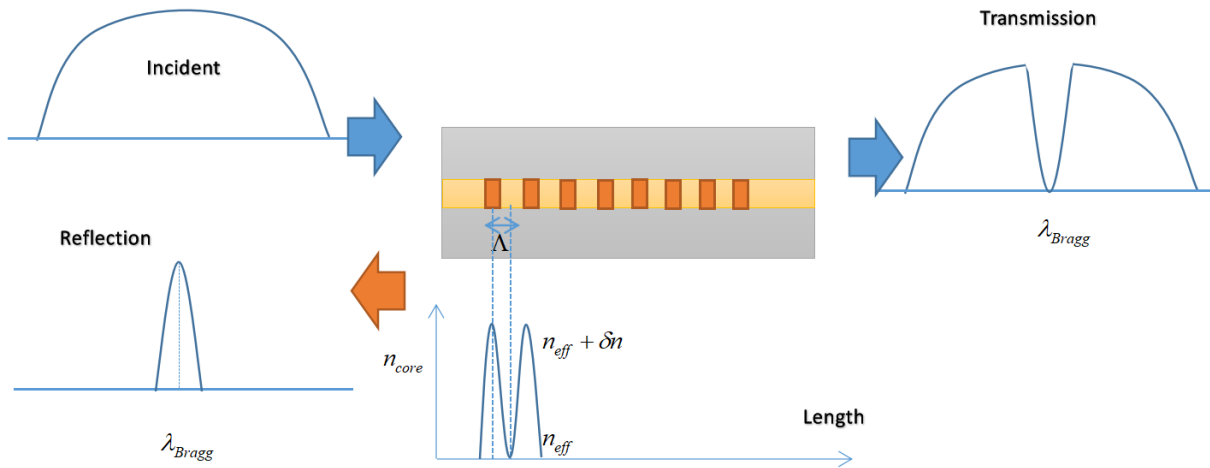
Figure 8 Operating Principles of Fiber Bragg Gratings

FBGs are interrogated with broadband light source and optical spectrum analyzer to obtain reflected spectrum. FBGs as sensors trace resonance wavelength by:

$$\frac{\Delta\lambda_{Bragg}}{\lambda_{Bragg}} = (1 - p_e)\varepsilon + (\alpha_\Lambda + \alpha_n)\Delta T \qquad (2.10)$$

where p_e is the strain optic coefficient, ε is strain, α_Λ is the thermal expansion coefficient, α_n is the thermo-optic coefficient. ΔT is temperature changing. The formula shows the feasibility for

FBGs to perform multi-parameter measurement. Another advantage of FBG is its flexibility in multiplexing compared with fiber interferometers. Gratings with different resonance wavelengths can be inscribed on one fiber. However, fabrication of FBGs normally involve higher cost than fiber interferometers due to its requirement of fabrication precision to produce periodical refractive index change with period ~0.5-1.0-μm.

2.3.1 Fiber Bragg Gratings Fabricated by Ultraviolet via Phase Mask

One approach to fabricate FBG is by ultraviolet (UV) exposure with a phase mask to form type-I grating refractive index change [10][11]. Figure 9 is a schematic sketch of the fabrication setup and Figure 10 is an actual photo. A cylindrical lens is placed between laser source and phase mask for spatial beam shaping. The phase mask is consisted of 10-15 sub-section of diffraction grating for FBG writing at different wavelengths. It is fabricated by E-beam lithography and react ion etching techniques on fused silica substrates. A beam of UV is split into two by each grating on phase mask and further cause interference on the fiber. Since cladding layer is transparent to UV, one sensor array is produced only on the core, consisting of 15-20 FBGs. Each FBG is 5-mm long and they are 10-mm spacing from each other.
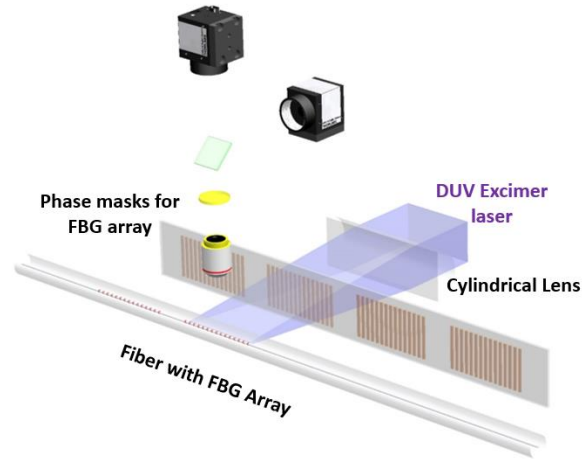
Figure 9 Schematic Sketch of Fabrication Setup of Fiber Bragg Gratings by Ultraviolet

Figure 10 Photo of Fabrication Setup of Fiber Bragg Gratings

The interference results of a single photon being absorbed by silica glass, which causes oxygen deficiency defect in silica glass. An increased refractive index change is formed. However, defect center will have reduced refractive index change in high temperature, which affects the functionality of FBGs since reflectivity is significantly deducted. Type-I FBGs are made of photosensitive optical fibers, such as Ge-doped silica glass [12]. The hydrogen pre-loading step

15

can significantly improve the photosensitivity of optical fibers. With hydrogen pre-loading, the reflectivity of this type of FBGs can approach up to 99.9%. Since light propagates in it with low loss and it can be fabricated with low cost, UV-inscribed FBG is the most widely used one.

2.3.2 Fiber Bragg Gratings Fabricated by Femtosecond Laser via Phase Mask

Femtosecond laser via phase mask technique is adopted as laser inscription tool to fabricate FBGs. This type of FBGs show their merit of ultra-high temperature stability. We take advantage of the second harmonic nonlinear photoluminescene excited by ultrafast laser pulses. Ultrafast laser exceeds the damage threshold of fiber to form type-II grating refractive index change at target materials. Permanent refractive index changes are formed. A Ti:Sapphire and amplifier system operates at 800-nm with repetition rate at 5 Hz. The laser pulses are focused into the fiber core using a cylindrical lens. The fiber is placed around 0.3-mm away from the phase mask along the beam propagation direction. A grating array is produced in the telecom band with a resonance wavelength at around 1525-nm [13].

One disadvantage of these FBGs is high loss of propagating light. Besides, the cost of the experimental setup is significantly higher than the previous one. These two reasons make type-II FBGs only suitable for specific applications.

2.3.3 Point-by-point Written Fiber Bragg Gratings

Another advanced technique to fabricate high temperature stable FBGs is point-by-point writing. It can drastically improve the manufacturing repeatability. Laser beam is focused into the fiber core from the flat surface. A specialty D-shape fiber is selected as platform. These fiber cores

are also doped with dopants like Ge. It will produce characteristics photoluminescene that is otherwise very weak without dopant in pure silica fiber cladding.

Figure 11 is a schematic sketch of ultrafast laser direct writing system. Due to curvature and diameter variation long cylindrical fiber, it is difficult to focus on laser beam into fiber core. A high-precision nonlinear microscopic imaging technique is adopted to locate the laser focus.
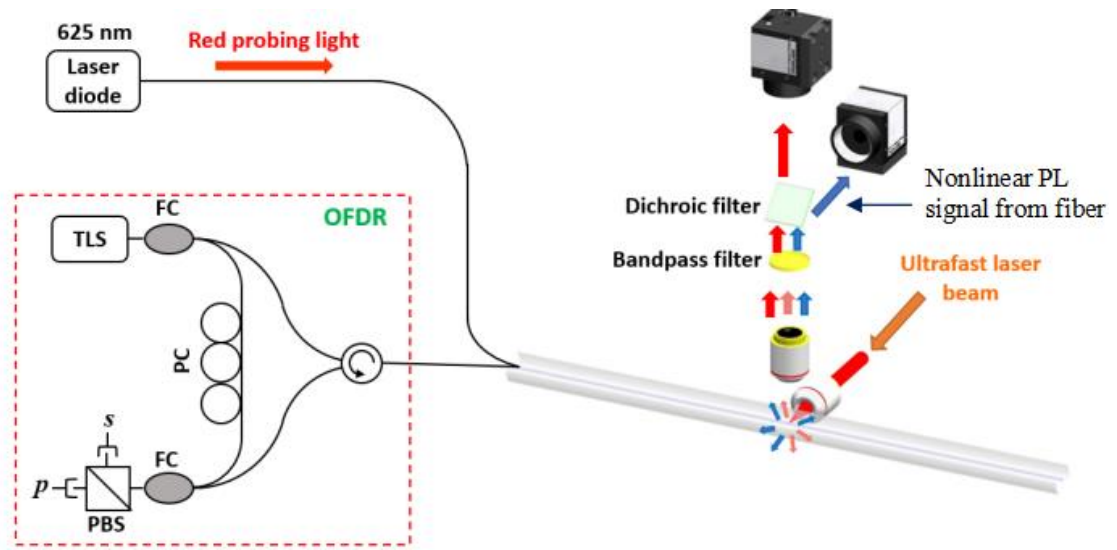
Figure 11 Schematic Sketch of Ultrafast Laser Processing

Second harmonic nonlinear photoluminescene signal is collected by a camera to provide a digital benchmark for maintaining the focal location. Meanwhile, a red-light beam is launched into the fiber and will be scattered by nano-gratings out of the core. This signal is collected by another camera. An optical frequency domain reflectometry (OFDR) system for real-time Rayleigh backscattering monitoring operates at 1550-nm. The scattered red-light signal (625-nm) and OFDR system develop a feedback control mechanism, which enables us to optimize the ultrafast laser enhanced Rayleigh backscattering profile of the fiber for improving the fabrication uniformity.

The period of inscribed grating is:

$$\Lambda = v_s / f_{rep} \qquad (2.11)$$

where v_s is moving speed of the stage and f_{rep} is repeated frequency of pulse train.

3.0 Demodulation of Intrinsic Fabry-Perot Interferometers

3.1 Fabrication and Characterization of Intrinsic Fabry-Perot Interferometers

Femtosecond laser processing is adopted as laser inscription tool to fabricate IFPIs. A standard telecom single mode fiber (Corning SMF-28+) is placed on a roll-to-roll fabrication setup [6]. The fabrication system is composed of a motion stage, a rotary stage, CCD cameras, 3-D print parts and mechanical pulleys. Figure 12 is a schematic sketch of the fabrication setup.
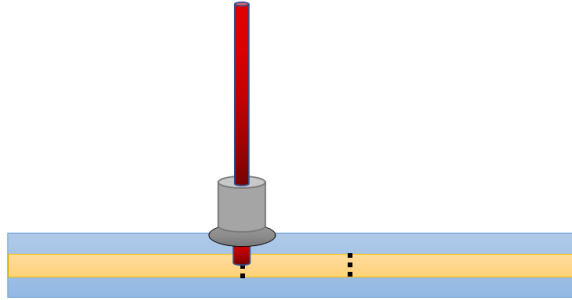
Figure 12 Schematic of Fabrication Setup for Intrinsic Fabry-Perot Interferometers

A Coherent RegA 9000 Ti:Sapphire laser and amplifier system operate at 800-nm, 270-fs with repetition rate at 250-kHz. Each reflector is created with 160-nJ on-target pulse energy. A beam of laser is focused on the core through an oil-immersion objective (Olympus 1 U-2B235, NA 1.25) for aberration compensation. A red light is launched into the fiber and scattered by nano gratings out of the core for observing the scattering profile of reflectors. Figure 13 shows scattering of red light at the reflector.
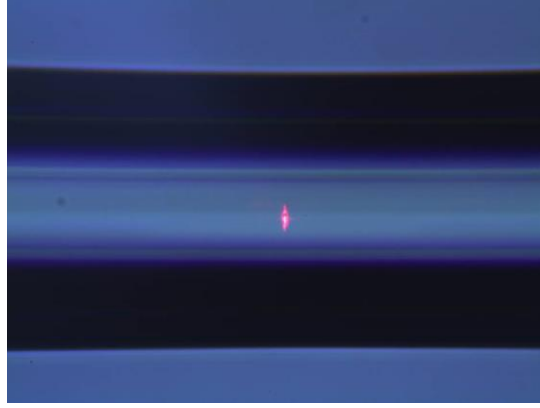
Figure 13 Scattering of Red Light at the Reflector

To verify locations of inscribed points, the fabrication is also characterized with an optical backscattering reflectometer (Luna OBR4600) for real time Rayleigh backscattering monitoring. Figure 14 is backscattering spectrum of an experiment sample cascaded of six sensors (All experiment data plotted with MATLAB R2018a).
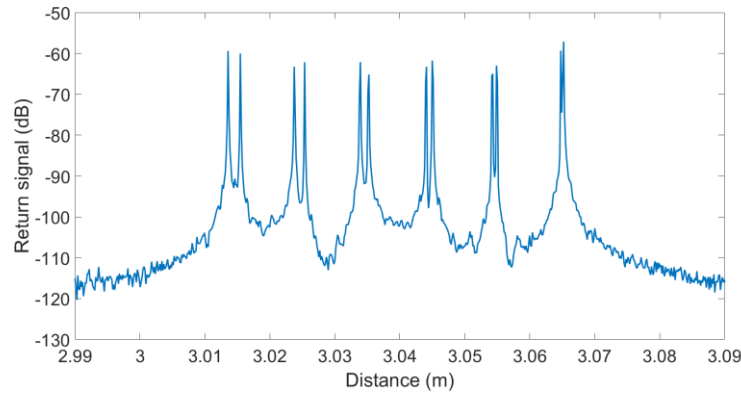
Figure 14 Rayleigh Backscattering of Multiplexed Intrinsic Fabry-Perot Interferometers

Figure 15 exhibits a schematic sketch of demodulation setup. A superluminescent light emitting diode (SLED, EXS210059-01) is used as light source. The SLED is coupled to the IFPI through a circulator. Interference spectrum is acquired by a spectrometer (FBGA, BaySpec Inc.)

with 512-element CMOS detector array with 156 pm/element resolution. The spectrometer has a

spectral range from 1510-nm to 1590-nm. The light source sweeps from 1510-nm to 1570-nm. 400

data points equally space according to wavelength with linear fit as Figure 16 shows. All data

points are interpolated and transformed from wavelength to wavenumber. Figure 17 depicts upper

and lower envelop of multiplexed IFPIs from 1520-nm to 1540-nm.
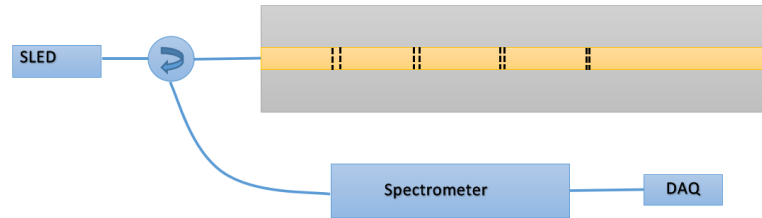
Figure 15 Schematic of Demodulation System for Intrinsic Fabry-Perot Interferometers
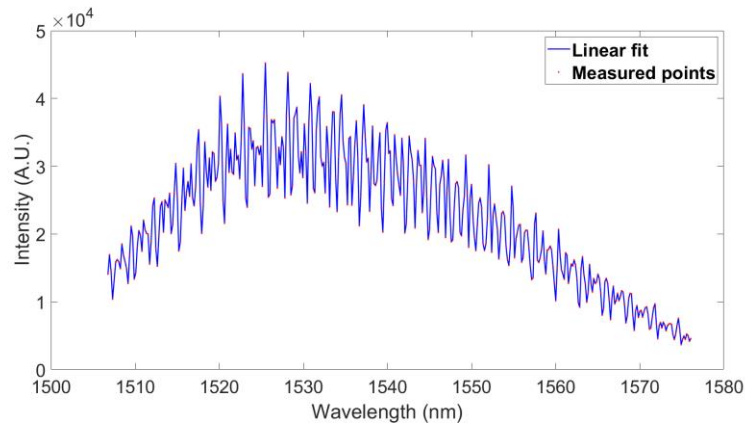
Figure 16 Reflected Intensity of Multiplexed Intrinsic Fabry-Perot Interferometers

21
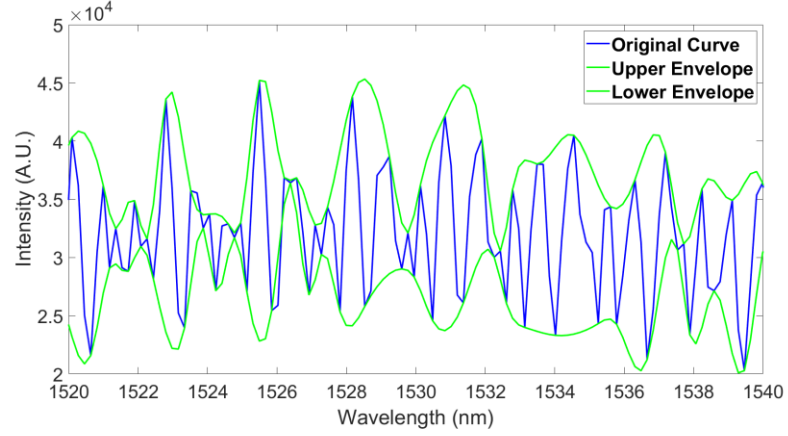
Figure 17 Envelopes of Intensity

Data points are transformed from wavelength to frequency by Fourier transform. Fourier transform is described as:

$$f(\tilde{\xi}) = \int_{-\infty}^{\infty} f(x) * e^{-2\pi i x \xi} dx \tag{3.1}$$

where x represents time, ξ represents frequency. Discrete Fourier transform (DFT) transforms finite discrete data from time domain to frequency domain by decomposing a sequence of values into components of different frequencies:

$$X_k = \sum_{n=0}^{N-1} x_n e^{-\frac{i2\pi}{N}kn} \tag{3.2}$$

Fast Fourier transform (FFT) is adopted as an optimized algorithm to implement DFT. It greatly deducts the computation volume by reusing the intermediate results. The original spectrum in FFT domain is symmetry. Only positive amplitude is selected. Data points are transformed from wavelength domain (Length = 2mm) into cavity length. Figure 18 clearly shows six peaks, which correspond to six sensors.

22
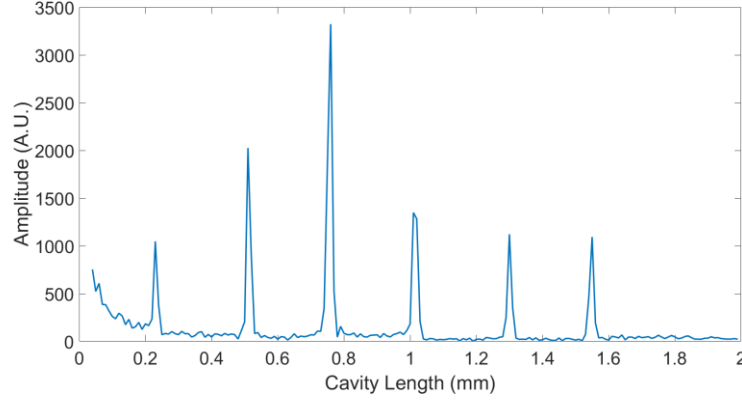
Figure 18 Amplitude in Cavity Length Domain

One frequently adopted approach to improve resolution of spectrum is to interpolate all data points with polynomials. Buneman frequency estimation (BFE) method is adopted as a rapid algorithm to localize the maximum function value from another point of view [14][15][16].

3.2 Buneman Frequency Estimation for Intrinsic Fabry-Perot Interferometers

3.2.1 Derivation of Buneman Formula

BFE algorithm aims to track the frequency of maximum value of a sinusoidal function when the underlying signal is not exactly periodic with the measured signal. As Figure 19 shows, discrete data points are fitted with conventional methods (blue line), such as polynomials. In that case, the data point n_p will be recognized as the maximum value of the whole sequence. In fact, since experimental data are measured discretely, hidden maximum value (red line) is likely to locate in a range, but not exactly on the data that we measured in spectrum. It will fall between

two measured adjacent maximum data points $F(n)$ and $F(n+1)$. BFE aims to determine the underlying value.
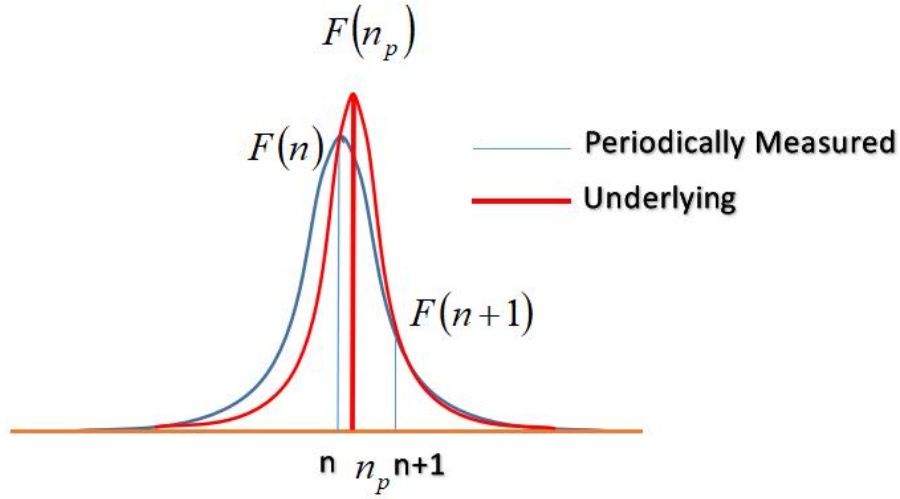
Figure 19 Principle of Buneman Frequency Estimation to Fit Underling Curve

To derive Buneman formula, measured data in spectrum (black line) is compared to DFT equation fit (blue line) [23] as Figure 20 exhibits. Given a function of sinusoidal signal by:

$$y = e^{i2\pi np/s} \tag{3.3}$$

where p is the location with respect to horizontal of the hidden maximum, s is resolution of the spectrum, n is the order of sequence. The DFT equation of this signal is by:

$$F(k) = \sum_{n=0}^{N-1} e^{i2\pi np/s} e^{-i2\pi ink/N} \tag{3.4}$$

$$F(k) = e^{i\pi(pN/s-k)(N-1)/N} \frac{sin[\pi(pN/s-k)]}{sin[\pi(pN/s-k)/N]} \tag{3.5}$$

where N is the volume of data, k is the order of sequence in DFT equation.
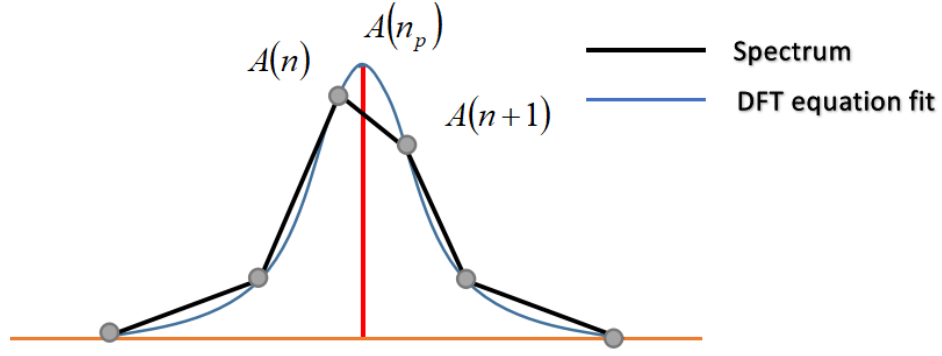
Figure 20 Comparison of Data Points in Spectrum and Discrete Fourier Transform Equation Fit

The Buneman formula can be derived from DFT equations of the two adjacent maximum data points by:

$$\frac{|F(n)|}{|F(n+1)|} = \frac{sin[\pi(pN/s-n)]/sin[\pi(pN/s-n)/N]}{sin[\pi(pN/s-(n+1))]/sin[\pi(pN/s-(n+1))/N]} \tag{3.6}$$

$$p = n + s\frac{N}{\pi}arctan\left[\frac{sin\frac{\pi}{N}}{cos\frac{\pi}{N}+\frac{|F(n)|}{|F(n+1)|}}\right] \tag{3.7}$$

3.2.2 Buneman Frequency Estimation for the Most Intense Amplitude

Optical cavity length can be calculated from the spectrum by:

$$l = \frac{2\pi n_p}{k_0-k_1} \tag{3.8}$$

where n_p is the fringe order in FFT domain, k_0 is wavenumber of the first data point, k_1 is wavenumber of the last data point. The first main step is to calculate a rough estimation FFT index $\tilde{n}_p$ with measured fringe orders. To eliminate direct current phase, the first 4 data points in FFT domain is removed. In FFT domain, resolution of spectrum is set to be 1, Buneman formula is by:

$$\tilde{n}_p = n + \frac{N}{\pi}\left[\frac{sin\frac{\pi}{N}}{cos\frac{\pi}{N}+\frac{A_n}{A_{n+1}}}\right] \tag{3.9}$$

25

If we use data presented in Figure 18 as an example, the demodulation of Sensor 3 with cavity length around 0.75 mm will involve 30 data points ($N = 30$). The roughly estimated FFT index $\tilde{n}_p = 76.356278$. This yield a cavity length of 763562.78-nm.

Since fringe orders result from constructive interference, the second step goes back to phase value, which is the origin of fringe orders. The all-phase analysis is indispensable for FFT spectrum. It is used to analyze the frequency spectrum of two sequences with delay relationship [17]. The time-shift phase difference can be corrected. The electric field envelope removing is also involved in this step by calculation [14]. It is achieved by averaging the phase of two adjacent points:

$$k'_0 = (k_0 + k_1)/2 \tag{3.10}$$

According to equation (2.8) and (3.10), light source is adapted by:

$$I'(k) = I_0(k + (k_0 + k_1)/2) \tag{3.11}$$

According to equation (2.8) and (3.11), the interference formula is by:

$$I(k) = 2I'(k + k_0 - (k_0 + k_1)/2)\left[1 + \gamma \cos(l(k + k_0)) + \phi_0\right] \tag{3.12}$$

According to equation (3.12), the positive amplitude in FFT domain is by:

$$I^+(\xi) = \gamma e^{i[\phi_0 - (k_0 - k_1)/2 + (k_0 + k_1)/2]} I'(\xi - l) \tag{3.13}$$

The distance between two points with respect to FFT index is by:

$$\Delta\xi = \frac{2\pi}{k_0 - k_1} \tag{3.14}$$

The phase value of a data point locating at ξ is the positive argument in equation (3.13), which is by:

$$\phi(\xi) = \phi_0 - (k_0 - k_1)/2 + (k_0 + k_1)/2 \tag{3.15}$$

According to equation (3.14) and (3.15), phase of the maximum amplitude at index n_p in all phase can be calculated with initial phase, which is by:

$$\phi(k_0) = \phi_0 + k_0 l = \phi_0 + \frac{2\pi n_p k_0}{k_0 - k_1} \qquad (3.16)$$

The first attempt to obtain all phase is with unwrapped spectrum. As Figure 21 shows, phase value has an overall downward trend with occasional fluctuations. Phase deducts from 0 to around -18π radian. The spectrum is zoomed in to show how the accurate result is localized more intuitively as depicted in Figure 22. Previously estimated index n_p falls on the slope between data points at 0.76-mm and 0.77-mm.
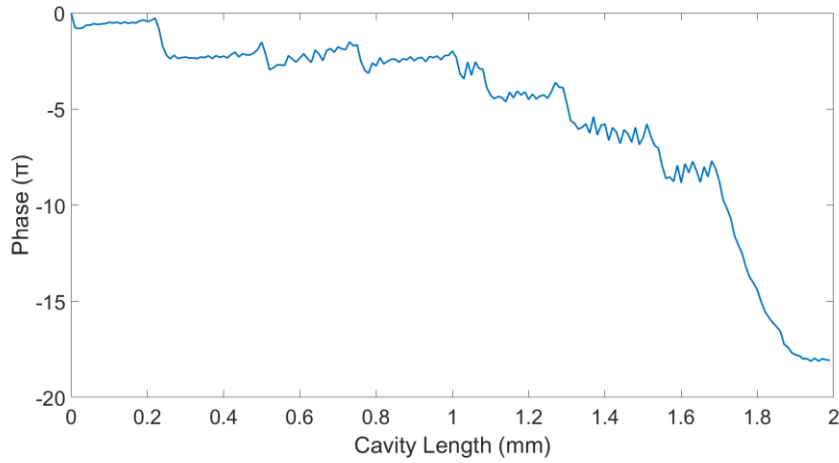
Figure 21 Unwrapped Phase Spectrum
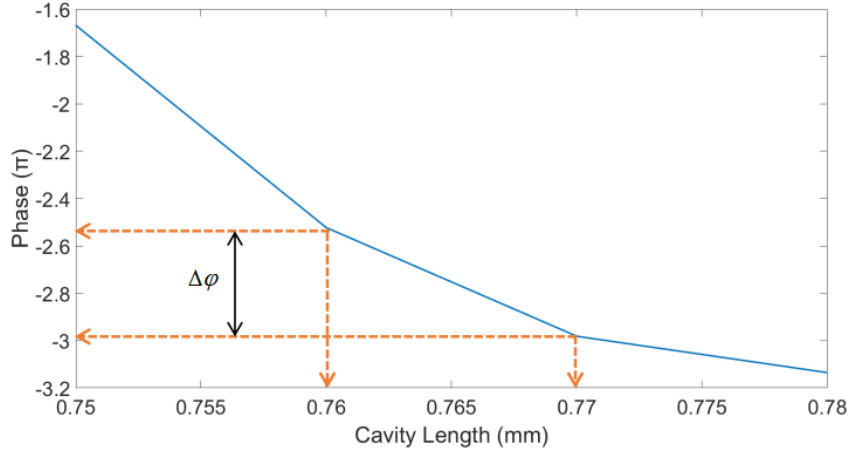
Figure 22 Phase Shift in Unwrapped Phase Spectrum

After obtaining the phase of data point n_p, the all-phase of a point locating at index n_p can be calculated with value of discrete data point locating at 0.76-nm plus the fractional component:

$$\phi_{n_p} = \phi_n + \Delta\phi(\tilde{n}_p - n) \qquad (3.17)$$

The accurate result is calculated with roughly estimated FFT index and wavenumber of the whole spectrum by:

$$n_p = \frac{k_0 - k_1}{k_0}\left[\phi_n + \Delta\phi(\tilde{n}_p - n)\right] \qquad (3.18)$$

However, the phase shift between two adjacent data points is not always a constant because extra error incurs. This can also be observed in unwrapped phase spectrum. It is unable to detect an accuracy phase value. After literature studying [18], a method is adopted to obtain all phase in wrapped phase spectrum as Figure 23 shows. It is mainly achieved by calculating the times phase value gets wrapped.

Figure 24 shows that phase difference of point 0.77-mm and 0.76-mm is $\sim -0.5\pi$, which is consistent with the one in unwrapped phase spectrum. The value of phase will keep the same when it shifts 2π or $2\pi a$ radian due to the nature of wrapping:

$$\phi_p = \phi_{n_p} + 2\pi a \qquad (3.19)$$

where a is wrapping time. All phase of a discrete data point is obtained with the measured one and wrapping time. According to equation (3.8), (3.17), (3.19), the wrapping time can be calculated with the consistence of wrapped and unwrapped phase value by:

$$a = \frac{k_0 \tilde{n}_p}{k_0 - k_1} + \frac{\phi_0 - \phi_n}{2\pi} - \frac{\Delta\phi(\tilde{n}_p - n)}{2\pi} \qquad (3.20)$$
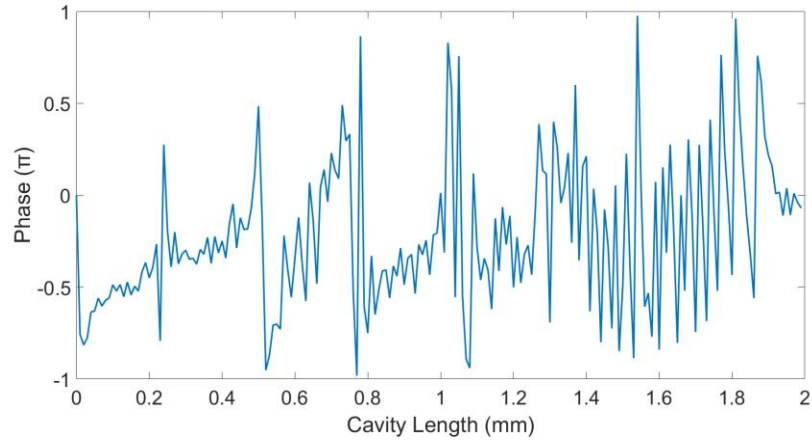
Figure 23 Wrapped Phase Spectrum
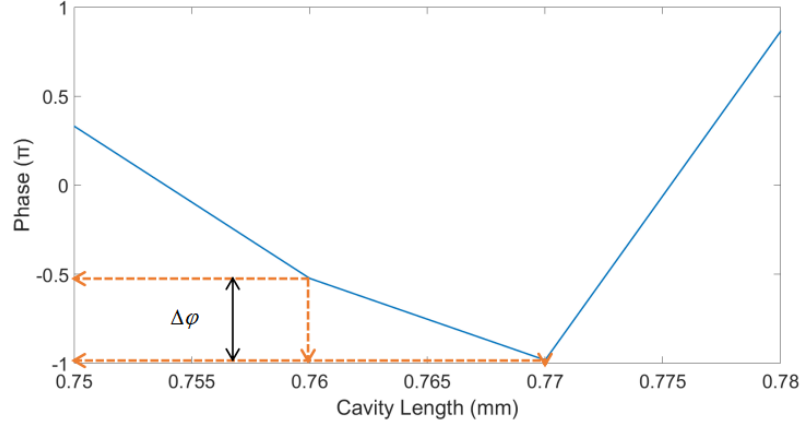
Figure 24 Phase Shift in Wrapped Spectrum

According to equation (3.17), (3.19) and (3.20), the accurate n_p is by:

$$n_p = \frac{1}{\frac{2k_0}{k_0-k_1}+1}\left(\frac{\phi_n-\phi_0}{\pi}+n+2a\right) \tag{3.21}$$

Given wavenumber of the first data point $k_0 = 0.00417$, wavenumber of the last data point $k_1 = 0.00399$, roughly estimated FFT index $\tilde{n}_p = 76.356278$, these yield an accurate cavity length of 763610.0-nm. Cavity lengths of Sensor 3 in 2 second are depicted in Figure 25.
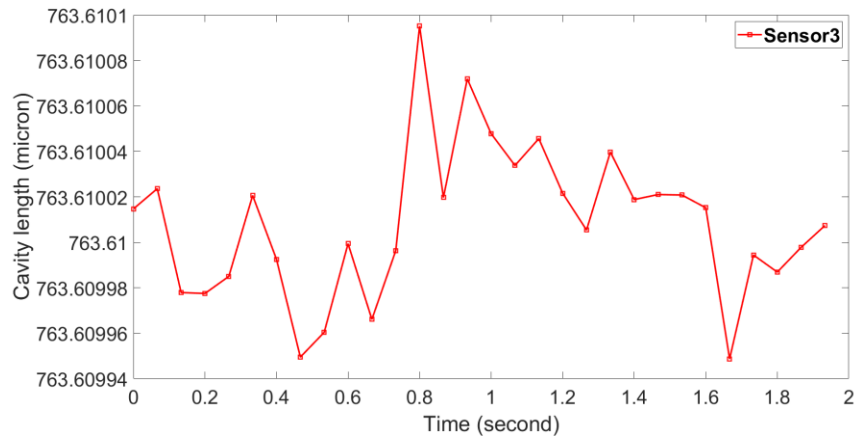
Figure 25 Cavity Length of the Most Intense Sensor

30

3.2.3 Buneman Frequency Estimation for Multi-points

Cavity lengths of six sensors at initial time are listed in Table 1. To show their variation, all cavity length differences are plotted in Figure 26. The range is less than 1-nm. The result is consistent with the fact that no artificial strain or temperature change is attached to IFPI. Change of cavity length should be extremely small but not a constant, given dust and air perturbation in the lab.

Table 1 Cavity Length Determined by Buneman Frequency Estimation Method at Initial Time

	Sensor 1	Sensor 2	Sensor 3	Sensor 4	Sensor 5	Sensor 6
Cavity length (nm)	252550.3	522933.8	763610.0	1024722.1	1312199.1	1553146.2
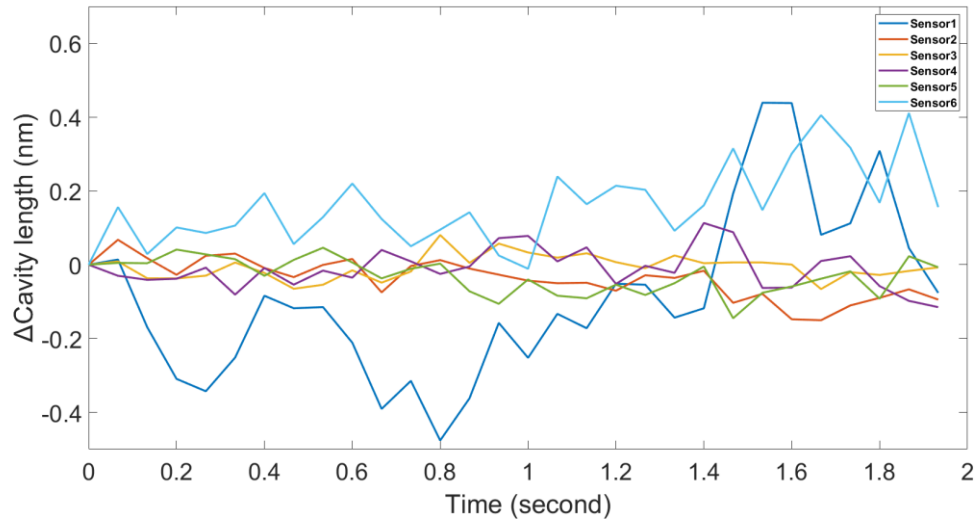
Figure 26 Cavity Length Differences

4.0 Demodulation of Fiber Bragg Gratings

4.1 Characterization of Fiber Bragg Gratings

The primary objective of this experiment is to quantitively evaluate irradiation resistance of FBGs in random air-line (Corning's RAL) fibers compared to FBGs in F-doped cladding single mode fibers (Corning's Vascade) with property drifts [13]. Only pure silica RAL fiber is demodulated in this thesis. FBGs are fabricated by femtosecond laser via phase mask. The result is carried out in MIT nuclear reactor lab. The nuclear reactor is with neutron and gamma irradiation and a temperature above $600°C$.

The sensors are slipped into a stainless-steel tube for protection. One end of the tube is sealed while the other is left open to allow fiber to connect with an FBG interrogation system. The FBG interrogation system is composed of a tunable laser (TUNICS T100S-HP Yenista Optics) and an optical switch (CT400 Yenista Optics). Data is acquired every 20 second with a bandwidth from 1440-nm to 1640-nm. Experiment data is selected every five days for resonance wavelength and linewidth analysis. As Figure 27 shows, FBG has the most intense return signal at initial time. Intensity degrades gradually because neutrons change the backscattering in the reactor core. Figure 28 shows reflected power spectrum at initial time.
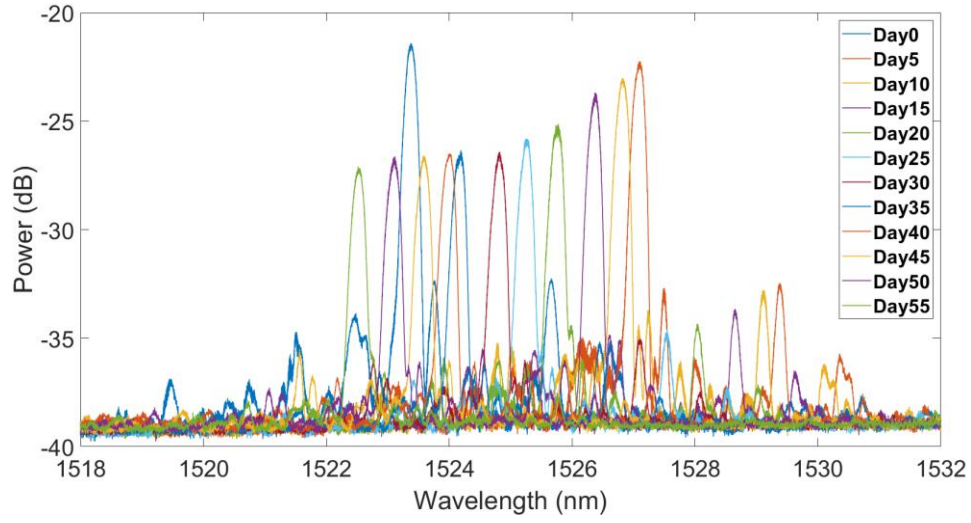
Figure 27 Power Spectrum of Fiber Bragg Gratings
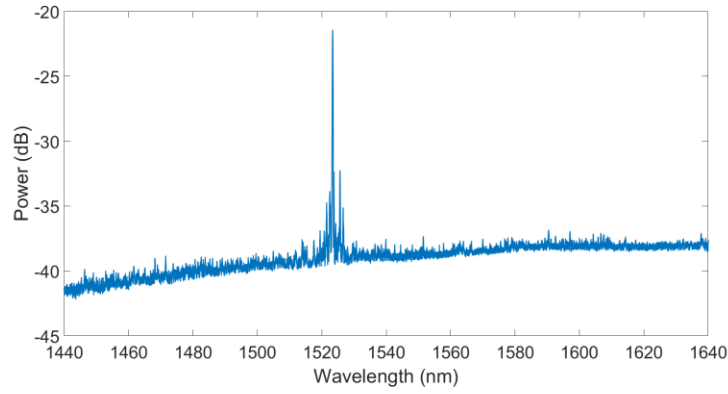
Figure 28 Power Spectrum at Initial Time

To focus on central peak, Side lobes are ignored. The ordinate is transferred from power to reflectivity by formulas below:

$$A = 10 \times log_{10} \frac{R_2}{R_1} \tag{4.1}$$

$$R_2 = R_1 \times 10^{A/10} \tag{4.2}$$

As Figure 29 shows, central peak locates approximately at 1523.4-nm. Three demodulation methods are adopted for fit determination and for comparison. They are Gaussian fit method, BFE algorithm and linear fit method.
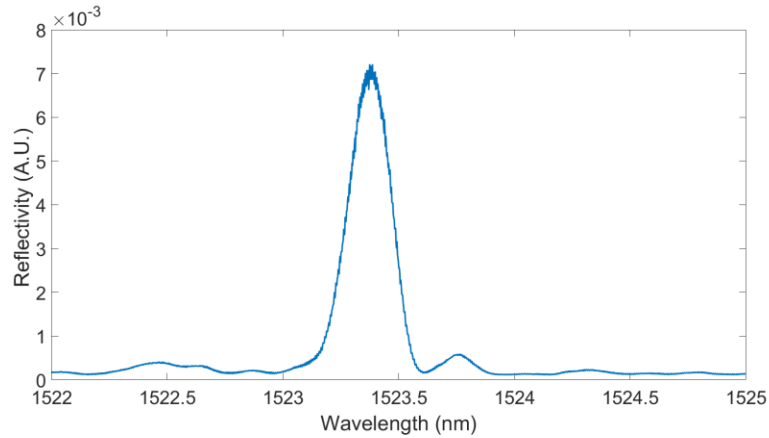
Figure 29 Zoom-in Reflectivity Spectrum at Initial Time

4.2 Bragg Wavelength Drift Analysis

FBGs as sensors work by tracing resonance wavelength. As depicted in Figure 30, peak reflectivity quickly moves toward longer wavelength because the reactor power is raised over of a period of 3 days to keep a steady power and stable temperature. Then, it moves toward shorter wavelength gradually because of temperature change. Meanwhile, intensities degrades gradually since nuclear irradiation changes backscattering in fiber core.

4.2.1 Bragg Wavelength Drift Determined by Buneman Formula

According to Yang [23], Buneman formula is adapted for FBG by:

$$\lambda_{Bragg} = \lambda_n + \lambda_r \frac{N}{\pi} arctan \left[\frac{sin\frac{\pi}{N}}{cos\frac{\pi}{N} + \frac{|R(\lambda_n)|}{|R(\lambda_{n+1})|}} \right] \tag{4.3}$$

where N is the volume of focused data points, $R(\lambda_n)$ denotes the maximum reflectivity, $R(\lambda_{n+1})$ is the second maximum reflectivity, λ_r is resolution of the spectrum, λ_{Bragg} is estimated Bragg wavelength. At initial time, volume of focused data points $N = 452$, reflectivity of the maximum data point $R(\lambda_n) = 0.0072 A.U.$, reflectivity of the second maximum data point $R(\lambda_{n+1}) = 0.0069 A.U.$, resolution of the spectrum $\lambda_r = 0.002nm$. This yields a resonance wavelength $\lambda_{Bragg} = 1523.37498nm$.

4.2.2 Bragg Wavelength Drift Determined by Gaussian Fit Method

In general, a weak FBG reflection spectrum can be fitted with a Gaussian function [19], which is a multiple step fitting algorithm that is sensitive to noise in the data. Figure 30 is a screenshot of using Curve Fitting Toolbox to fit data with a Gaussian function.
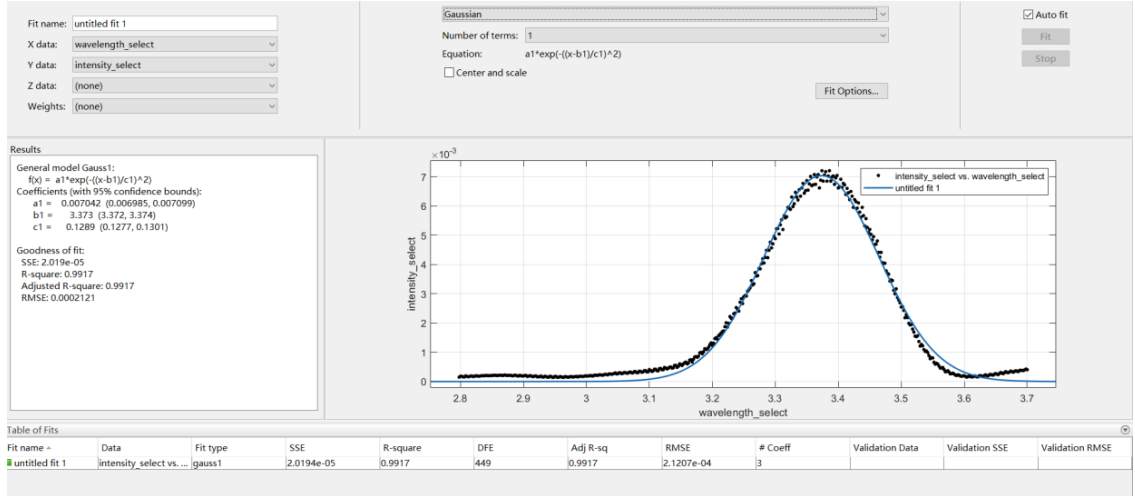
Figure 30 Screenshot of Applying Gaussian Fitting

The Gaussian function is by:

$$f(x) = ae^{-\frac{(x-b)^2}{2c^2}} \tag{4.4}$$

where a denotes amplitude, b is central location of the peak, c is related to peak width. To improve resolution, all calculated results are deducted by 1520-nm before implementing Gaussian fit method since software only keeps 4 significant digits. Number of terms is set as 1. As Figure 30 shows, the value b is determined as 3.373 at initial time, which yields a resonance wavelength at 1523.373-nm. The analysis of drifts starts at day 5 since nuclear reactor power keeps constant at Day 3. Demodulated results are depicted in Figure 31. Bragg wavelength moves toward shorter wavelength because temperature in the reactor decreases gradually. The calculated result states that resonance wavelength has drift 4.58-nm in total with an average speed of 91.6-pm/day with linear fit method.

36
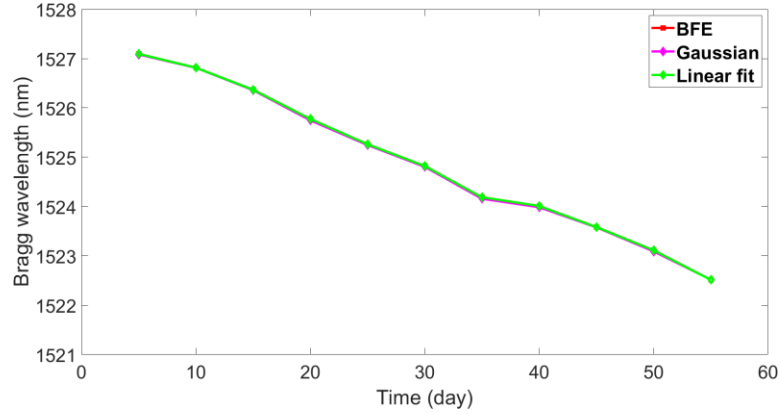
Figure 31 Resonance Wavelength Drifts

It is difficult to determine their differences directly in Figure 34 since representing lines of three methods almost overlap. To achieve this objective, the variances of Gaussian fit method and linear fit method are calculated and depicted in Figure 32. It has an average value around $5 \times 10^{-4} nm^2$. The variances of BFE method and linear fit method are depicted in Figure 33. It has an average value around $9.5 \times 10^{-7} nm^2$. Both values are rather small. However, the variance between BFE method and linear fit is three orders of magnitude smaller than the other one. The result implies that these two methods do not have large deviation to linear fit method but BFE algorithm has much higher precision than Gaussian fit method in this case.
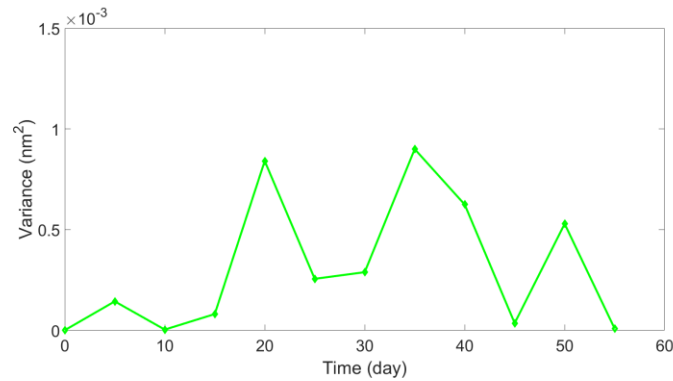
Figure 32 Variances of Gaussian Fit Method and Linear Fit Method

37
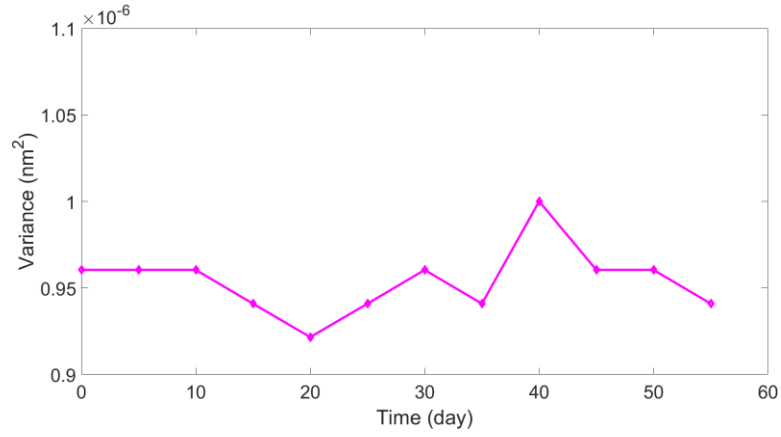
Figure 33 Variances of Buneman Frequency Estimation Method and Linear Fit Method

4.3 Linewidth Analysis

Another studied parameter is full width at half maximum (FWHM). The conception is depicted in Figure 34. In general, FWHM examines resolution of the spectrum. In this experiment, FWHM refers to full width of wavelength at half maximum intensity. A small value of linewidth is expected so that it can bring stability to sensing applications.
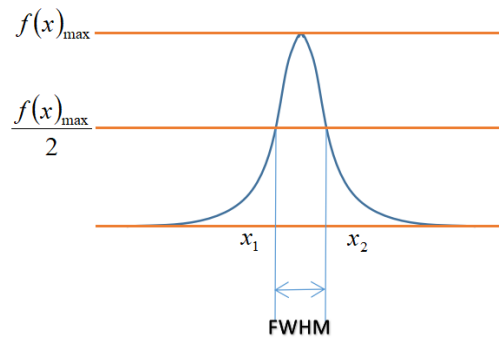
Figure 34 Definition of Full Width at Half Maximum

4.3.1 Full Width at Half Maximum Determined by Buneman Frequency Estimation Method and Linear Fit Method

Half maximum intensities can be directly calculated with obtained peak values for both linear fit method and BFE method while the calculations of width are different. As for linear fit method, since all data are interpolated with a line, corresponding wavelength can be acquired from that line. Since it is unlikely to obtain exact wavelengths with respect to half intensity, two nearest wavelengths are adopted for BFE algorithm for width calculation.

4.3.2 Full Width at Half Maximum Determined by Gaussian Fit Method

FWHM determined by Gaussian fit method is by:

$$FWHM = 2\sqrt{2\,ln\,2}\,c \approx 2.35482c \qquad (4.5)$$

where c is a given value. FWHM values of three methods are calculated and depicted in Figure 35. The ranges vary within 0.4-nm. At initial time, FWHM determined by Gaussian fit method has the smallest value of 0.30354-nm. FWHMs determined by BFE method and linear fit method are 0.2060-nm and 0.2080-nm, respectively, which are very close.
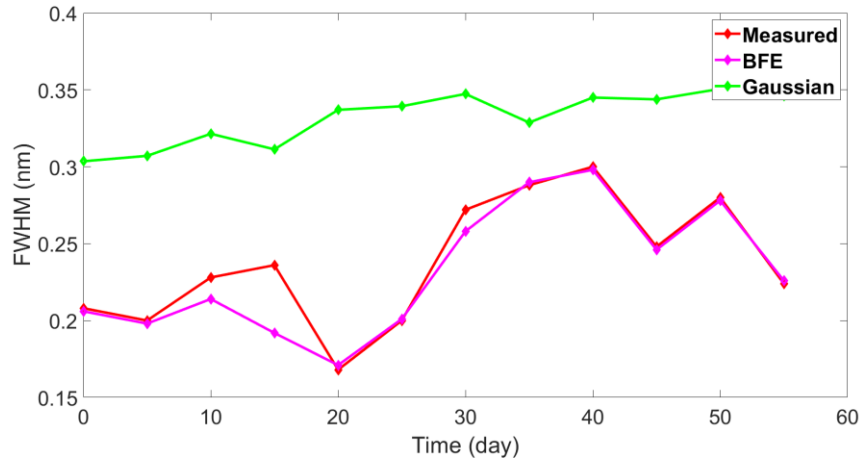
Figure 35 Variation of Full Width at Half Maximum

To quantitively evaluate stability of FWHMs. FWHMs are calculated as difference values compared with initial time and depicted in Figure 36. FWHM differences of linear fit method, BFE method and Gaussian fit method are determined to have average variation of 29.7-pm, 25.5-pm, 28.2-pm, respectively.
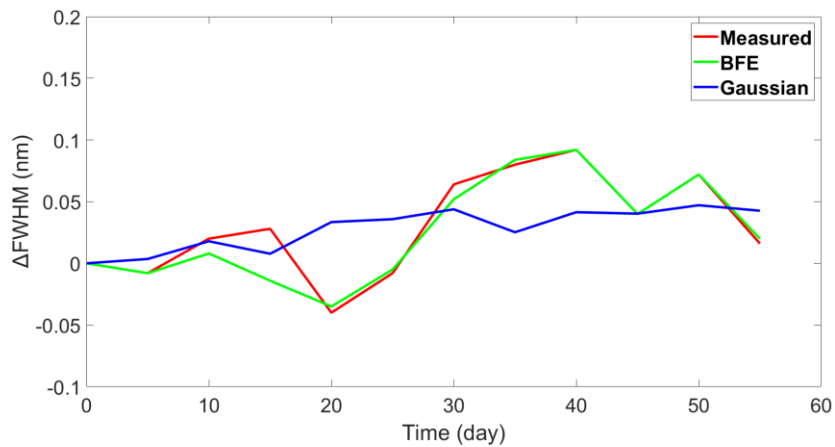
Figure 36 Full Width at Half Maximum Differences

Variances of three methods and their own average values are depicted in Figure 37. Both BFE method and linear fit method have average value around $2 \times 10^{-3} nm^2$. Gaussian fit method has an average value less than $1 \times 10^{-3} nm^2$. It implies that though Gaussian fitting method results of the largest linewidth, it has the highest stability of linewidth.

Figure 37 Variance of Three Methods and Their Average Values

With the results, we conclude that resonance wavelength of FBGs moves toward shorter wavelength when external temperature reduces. But linewidth of 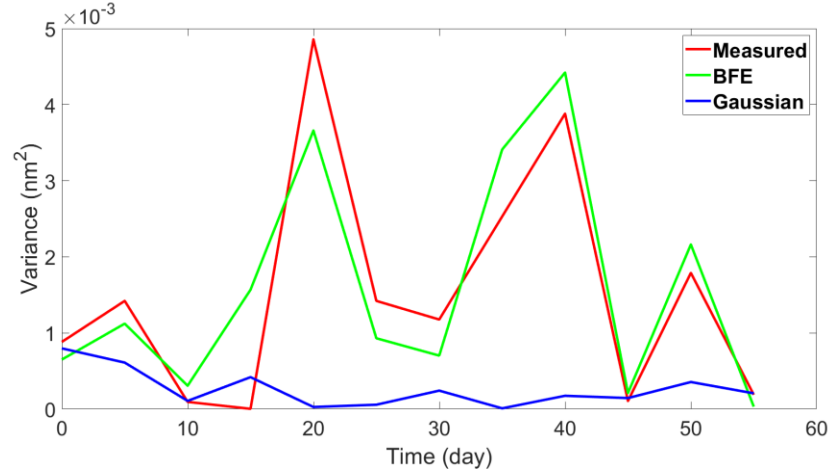the same FBGs do not change with respect to variation of temperature. The result is consistent with the phenomena reported by Chang [20], Morey [21] and Fan [22] that FWHM of a femto-laser inscribed FBG is independent on temperature. It is worth noting that the examined linewidth leads a potential approach to measure parameters other than temperature, such as stress [28]. Since linewidth with respect to both temperature and stress $FWHM_{\mu+T}$ is proportional to external stress while linewidth with respect to temperature only $FWHM_T$ is a constant, measurement of temperature and stress can be achieved with variation of $FWHM_{\mu+T}$ and Bragg wavelength drift of a single FBG.

5.0 Conclusion

In this thesis, I reviewed operating principles of optical fibers and fabrication techniques to engineer optical fibers into sensing devices. An optimized combination of fiber selections and fabrication techniques would be indispensable for optical sensing applications. However, there is no given answer for each condition. It is always a trade-off between performance and demand. Ultrafast laser processing was adopted in these experiments so FOSs could withstand ultra-high temperature. However, as for civil engineering application, UV-inscribed FBGs would be an economical choice.

In terms of demodulation, Buneman frequency estimation was adopted for IFPIs to distinguish multiple fringe orders. Resolution increased by orders of magnitude. Wrapped spectrum was adopted for all-phase analysis to avoid extra error. Variation of optical cavity length was smaller than 1-nm.

The algorithm was also compared with Gaussian peak fit method to determine resonance wavelength drift of FBGs. The result showed that BFE algorithm produce better both FBG and IFPI sensor demodulation results with 3 times less variance than Gaussian fit method. With BFE method, FWHM of the spectrum was determined at round 0.2-nm. Quantified FWHM differences and resonance wavelength drifts showed a potential approach to detect parameters other than temperature.

One advantage of BFE algorithm is it greatly reduces the cost of demodulation setup. The demodulation system can be composed of low-resolution interrogation schemes like a tunable laser or spectrometers with low spatial resolution. More importantly, this algorithm significantly deducts computation power compared to either polynomials or Gaussian function since only few

data points are acquired to achieve the whole demodulation. With set software program (e.g. LabVIEW, MATLAB), it is practical to perform real-time detection on remote.

Research results presented in this thesis clearly shows that the modified Bunman frequency estimation method can produce consistent and high accuracy demodulation results for fiber sensors. However, this approach can still be improved. First, in the future, this method should be implemented directly into digital signal processing (DSP) chip for real-time sensor spectral demodulation at different spectral frame rates for both FBG and IFPI sensor array with different sensor counts. Through large scale tests in various scenarios, we will further refine computational algorithm to produce stable and consistent results.

A more important future research approach is to improve the adaptability of the algorithm. In many situations, laser writing or extreme temperature could significantly change sensor spectra. For examples, extreme sensor annealing could reduce FBG peak and yield strong side lopes. This will create a sensor with more than one reflection peak. This will prevent the algorithm to make accurate estimation of the sensor peaks. This is a common issue for many sensors, especially when these sensors have endured long period of time in harsh environment. This improvement can be achieved by an integrated solution while the original spectra of sensors are "memorized" by the algorithm and used to perform initial fitting of the spectral. The Bunman algorithm will then be applied only to the portion of spectral for accurate peak determination. This improvement will greatly improve applicability of this work.

Bibliography

[1]   Choi H.Y., Park K.S., Park S.J., Paek U.C., Lee B.H., Choi E.S. Miniature fiber-optic high temperature sensor based on a hybrid structured Fabry-Perot interferometer Opt. Lett., vol. 33, no. 21, pp. 2455-2457, 2008.

[2]   Wang A, Miller MS, Plante AJ, Gunther MF, Murphy KA, Claus RO. Split-spectrum intensity-based optical fiber sensors for measurement of microdisplacement, strain, and pressure. Appl. Opt., vol. 35, no. 15, pp. 2595-2601, 1996.

[3]   J. Zheng, W. Li and X. Liu, "Fast and simple interrogation of extrinsic Fabry-Perot interferometer sensor based on dual-wavelength intensity ratio," Optics Communications, vol. 439, pp. 176-180, 2019.

[4]   Z. Chen, L. Yuan, G. Hefferman, and T. Wei, "Ultraweak intrinsic Fabry–Perot cavity array for distributed sensing," Opt. Lett., vol. 40, no. 3, pp. 320-323, 2015.

[5]   R. Osellame, G. Cerullo, and R. Ramponi (Editors), Femtosecond laser micromachining: photonic and microfluidic devices in transparent materials. Heidelberg: Springer-Verlag, 2012.

[6]   M. Wang, Y. Yang, S. Huang, J. Wu, K. Zhao, Y. Li, Z. Peng, R. Zou, H. Lan, P. R. Ohodnicki, P. Lu, M. Buric, Bo Liu, Q. Yu, and K. P. Chen, "Multiplexable High-Temperature Stable and Low-loss Intrinsic Fabry-Perot In-fiber Sensors through Nanograting Engineering," Optics Express, vol. 28, no. 14, pp. 20225-20235, 2020.

[7]   Flores, R., Janeiro, R. & Viegas, J. Optical fibre Fabry-Pérot interferometer based on inline microcavities for salinity and temperature sensing. Sci. Rep., no. 9, pp. 41598-45909, 2019.

[8]   Saleh, B. E. A. & Teich, M. C., Fundamentals of Photonics. Hoboken: Wiley-interscience, 2007.

[9]   K. O. Hill, Y. Fujii, D. C. Johnson, and B. S. Kawasaki. Photosensitivity in optical fiber waveguides: Application to reflection filter fabrication. Applied Physics Letters, vol. 32, no. 10, pp. 647-649, 1978.

[10]   G. Meltz, W. W. Morey, and W. H. Glenn. Formation of bragg gratings in optical fibers by a transverse holographic method. Opt. Lett., vol. 14, no. 15, pp. 823-825, 1989.

[11]   R. Kashyap, J.R. Armitage, R. Wyatt, S.T. Davey, and D.L. Williams. All-fibre narrowband reflection gratings at 1500 nm. Electronics Letters, vol. 26, no. 11, pp. 730-732, 1990.

[12]   Oleg I. Medvedkov, Sergei A. Vasiliev, Pavel I. Gnusin, and Evgeny M. Dianov, "Photosensitivity of optical fibers with extremely high germanium concentration," Opt. Mater. Express, vol. 2, no. 11, pp. 1478-1489, 2012.

[13]   M. A. S. Zaghloul, M. Wang, S. Huang, C. Hnatovsky, D. Grobnic, S. Mihailov, M-J. Li, D. Carpenter, L-W. Hu, J. Daw, G. Laffont, S. Nehr, and K. P. Chen, "Radiation Resistant Fiber Bragg Grating in Random Air-line Fibers for Sensing Applications in Nuclear Reactor Cores," Optics Express, vol. 26, no. 9, pp. 11775-11786, 2018.

[14]   Z. Yu and A. Wang, "Fast white light interferometry demodulation algorithm for low-finesse Fabry–Pérot sensors," IEEE Photonics Technol. Lett., vol. 27, no. 8, pp. 817-820, 2015.

[15]   Z. Yu and A. Wang, "Fast demodulation algorithm for multiplexed low-finesse Fabry–Perot interferometers," J. Lightwave Technol., vol. 34, no. 3, pp. 1015-1019, 2016.

[16]   Y. Yang, E. Wang, K. Chen, Z. Yu, and Q. Yu, "Fiber-optic Fabry–Perot sensor for simultaneous measurement of tilt angle and vibration acceleration," IEEE Sens. J., vol. 19, no. 6, pp. 2162-2169, 2019.

[17]   Z. H. Wang, Z. X. Hou, and F. Su, "All phase FFT spectrum analysis," Journal of China Institute of Communications, vol. 24, no. 11A., pp. 16-20, 2003.

[18]   Y. Yang, J. Wu, M. Wang, Q. Wang, and K. P. Chen, "Fast Demodulation of Fiber Bragg Grating Wavelength from Low-resolution Spectral Measurements using Buneman Frequency Estimation," Journal of Lightwave Technology, vol. 38, no. 18, pp. 5142-5148, 2020.

[19]   T. Bodendorfer, M. S. Muller, F. Hirth and A. W. Koch, "Comparison of different peak detection algorithms with regards to spectrometic fiber Bragg grating interrogation systems," 2009 International Symposium on Optomechatronic Technologies, Istanbul, pp. 122-126, 2009.

[20]   C. C. Chang and S. T. Vohra, "Spectral broadening due to non-uniform strain fields in fibre Bragg grating based transducers," Electron. Lett., vol. 34, no. 18, pp. 1778-1779, 2002.

[21]   W. W. Morey, G. Meltz, and J. M. Weiss, "Recent advances in fiber-grating sensors for utility industry applications," Proceedings of SPIE - The International Society for Optical Engineering, pp. 90-98, 1996.

[22]   Fan Z, Diao X, Liu M, Zhang Y, Huang Z, Yan H. On-line monitoring of sealing glass in electrical penetration assembly based on femto-laser inscribed fiber Bragg grating sensors. Optics Express., vol. 27, no.2, pp. 608-620, 2019.